

Switchable Giant Spin Injection Current in Janus Altermagnet Fe₂SSeO

Fanxian Pei,^{1,2} Run-Wu Zhang,^{1,2,*} Lei Li,^{3,4,5,†} Dan Li,⁵ and Yugui Yao^{1,2}

¹Key Lab of advanced optoelectronic quantum architecture and measurement (MOE),
Beijing Key Lab of Nanophotonics & Ultrafine Optoelectronic Systems,
and School of Physics, Beijing Institute of Technology, Beijing 100081, China

²International Center for Quantum Materials, Beijing Institute of Technology, Zhuhai, 519000, China

³Research Center for Quantum Physics and Technologies,
Inner Mongolia University, Hohhot 010021, China

⁴Inner Mongolia Key Laboratory of Microscale Physics and Atomic Manufacturing,
Inner Mongolia University, Hohhot 010021, China

⁵School of Physical Science and Technology, Inner Mongolia University, Hohhot 010021, China
(Dated: December 22, 2025)

Generating and controlling spin current in miniaturized magnetic quantum devices remains a central objective of spintronics, due to its potential to enable future energy-efficient information technologies. Among the existing magnetic phases, altermagnetism have recently emerged as a highly promising platform for spin current generation and control, going beyond ferromagnetism and antiferromagnetism. Here, we propose a symmetry-allowed spin photovoltaic effect in two-dimensional (2D) altermagnetic semiconductors that enables predictable control of giant spin injection currents. Distinct from parity-time- (\mathcal{PT})-antiferromagnets, Janus altermagnetic semiconductors generate not only shift current but also a unique injection current with spin momentum locked in a specific direction under linearly polarized light—a mechanism absent in \mathcal{PT} -antiferromagnets. Through symmetry analysis and first-principles calculations, we identify Janus Fe₂SSeO as a promising candidate. Specifically, the monolayer Fe₂SSeO exhibits a polarization-dependent injection conductivity reaching $\sim 1,200 \mu\text{A}/\text{V}^2 \cdot \hbar/2e$, and the giant spin injection current can be effectively switched by rotating the magnetization direction and engineering strains. These findings underscore the potential of 2D altermagnets in spin photovoltaics and open avenues for innovative quantum devices.

Introduction.— The development of next-generation spintronics [1, 2] fundamentally depends on resolving a core challenge [3–5]: identifying capable materials of efficiently generating and controlling spin currents to enable energy-efficient spin-based technologies. Over the past decade, many spin-dependent transport phenomena have advanced the field, drawing widespread interest from both fundamental and applied perspectives [6, 7]. Nevertheless, the ultimate goal of achieving highly controllable spin currents remains elusive. Current approaches to spin current generation utilize various physical mechanisms, such as the spin Hall effect [8–10] in metals or the quantum spin Hall effect [11–13] in topological insulators. However, these methods suffer from two major limitations: the first concerns the narrow range of candidate materials, which are typically restricted to non-magnetic heavy metals with strong spin-orbit coupling, ferromagnets that produce stray fields, or parity-time- (\mathcal{PT})-symmetric antiferromagnets [5, 14–22] with spin polarizations that are difficult to harness; the second involves their general reliance on electrode contacts and their limited response times, typically on the nanosecond scale or slower. The former severely constrains material selection, excluding systems based on light elements or unconventional spin-splitting antiferromagnets. More importantly, the latter—namely the inherent need for electrical contacts and intrinsically restricted switching speeds—currently precludes the generation of spin currents in a contact-free, ultrafast manner.

Recent advances [23–33] in altermagnetic materials provide a promising pathway to overcome these challenges. Uniquely positioned at the intersection of desirable electronic properties, intrinsic lattice anisotropy, and efficient coupling with optical fields, altermagnets merge the advantages of ferromagnets and \mathcal{PT} -antiferromagnets while circumventing their key limitations, including dependence on heavy elements, unwanted stray fields, and inefficient spin utilization. More significantly, through the nonlinear photogalvanic effect [34–40], which is governed by distinctive time-reversal symmetry (\mathcal{T}) and \mathcal{PT} symmetry [41–44] properties that give rise to shift and injection currents [45, 46], altermagnets enable contact-free, ultrafast spin current generation with tailored optical polarization. These attributes establish altermagnets, especially two-dimensional (2D) altermagnets, not only expand the material paradigm for desired materials but also pave the way for optical spintronic devices operating without electrical contacts at unprecedented speeds.

In this work, we propose a distinct spin photogalvanic effect (SPVE) that enables predictable control of giant spin injection currents in 2D Janus altermagnets, simultaneously overcoming the two major limitations of conventional spin current generation schemes. We first elucidate the fundamental differences in spin photocurrent generation mechanisms between \mathcal{PT} -antiferromagnets and altermagnets in two dimension. Unlike \mathcal{PT} -antiferromagnets, altermagnets support not only shift

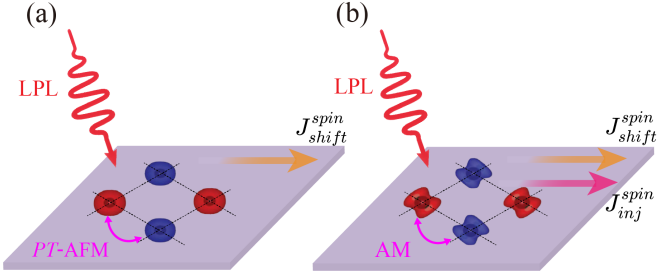


FIG. 1. Schematic of spin current generation by linearly polarized light (LPL) in (a) \mathcal{PT} -AFM and (b) AM. Unlike \mathcal{PT} -AFM, which is restricted to a spin shift current by \mathcal{PT} -symmetry, AM breaks \mathcal{P} , \mathcal{T} , and \mathcal{PT} , enabling both spin shift and spin injection currents simultaneously.

currents but also unique injection currents exhibiting specific spin-momentum locking under linearly polarized light illumination. We further demonstrate that Janus Fe_2SSeO monolayer hosts switchable giant spin injection currents through magnetization rotation and strain engineering. Remarkably, the Fe_2SSeO monolayer achieves a polarization-dependent injection conductivity of approximately $1200 \mu\text{A}/\text{V}^2 \cdot \hbar/2e$. Our findings not only provide desired material platform for exploring SPVE but also offer new opportunities for developing low-dimensional altermagnetic quantum devices.

Spin injection currents in 2D altermagnets.— The SPVE refers to the generation of a pure spin current under light illumination. When a material is irradiated with light of frequency ω , nonlinear optical (NLO) processes can generate a direct-current spin current described by the following expression:

$$j_{\text{dc}}^{c,s^i} = \sum_{\Omega=\pm\omega} \sigma_{ab}^{c,s^i} (0; \Omega, -\Omega) E_a(\Omega) E_b(-\Omega), \quad (1)$$

where $E(\omega)$ is the Fourier component of the electric field at angular frequency ω , σ denotes the NLO spin conductivity, c indicates the flow direction of the spin current, a and b specify the polarization directions of the electric field, and s^i ($i = x, y, z$) labels the spin polarization direction. Akin to the bulk photovoltaic effect (BPVE) [45, 47], which comprises shift and injection current contributions, the SPVE can similarly be decomposed into these two components. The shift current arises from the change in electron position during interband transitions, while the injection current originates from the change in electron velocity. Under a point-group symmetry operation R , a vector transforms as $r_a \rightarrow r'_a = \sum_b \mathcal{D}(R)_{ab} r_b$ [48]. Accordingly, the transformation [42, 49] of the fourth-rank spin conductivity tensors under linearly polarized light in Eq. (1) is given

by

$$\begin{aligned} \sigma'_{\text{shift,L}}{}^{c_1,s^i_1;a_1b_1} &= (-1)^{s^T} \det(R) \sum_{a,b,c,i} \mathcal{D}(R)_{c_1c} \mathcal{D}(R)_{i_1i} \\ &\quad \times \mathcal{D}(R)_{a_1a} \mathcal{D}(R)_{b_1b} \sigma_{\text{shift,L}}^{c,s^i;ab}, \\ \sigma'_{\text{inj,L}}{}^{c_1,s^i_1;a_1b_1} &= \det(R) \sum_{a,b,c,i} \mathcal{D}(R)_{c_1c} \mathcal{D}(R)_{i_1i} \mathcal{D}(R)_{a_1a} \\ &\quad \times \mathcal{D}(R)_{b_1b} \sigma_{\text{inj,L}}^{c,s^i;ab}. \end{aligned} \quad (2)$$

Note that for a symmetry operation that includes time reversal, we have $(t, r_a) \rightarrow (t', r'_a) = ((-1)^{s^T} t, \sum_b \mathcal{D}(R)_{ab} r_b)$. The factor of determinant $\det(R)$ appears in above transformation of spin-related quantities because spin is an axial vector.

As is evident from Eq. (2), broken spatial inversion symmetry (\mathcal{P}) is necessary for the SPVE to occur, while the specific form of the resulting spin current—whether shift or injection mechanism—is determined by the material's magnetic structure. Specifically, \mathcal{PT} symmetry will prohibit the tensor $\sigma_{\text{inj,L}}^{c,s^i;ab}$ while permitting $\sigma_{\text{shift,L}}^{c,s^i;ab}$. The explicit form of these conductivity tensors are provided in Section II of Supplementary Material (SM). In \mathcal{PT} -antiferromagnets, the spin-up and spin-down sublattices are related by the combined \mathcal{PT} operation, which allows the generation of a shift spin current under linearly polarized light. In altermagnets, by contrast, the opposite spin sublattices are connected by mirror-rotation (\mathcal{O}) symmetries. This breaks \mathcal{P} , \mathcal{T} , and \mathcal{PT} symmetries, allowing both shift and injection currents to emerge simultaneously under linear polarization, as depicted in Fig. 1.

Moreover, in real 2D magnetic systems, the Mermin-Wagner theorem [50, 51] prohibits spontaneous symmetry breaking at finite temperatures, in contrast to their three-dimensional (3D) counterparts. This fundamental constraint makes a relativistic analysis essential for understanding the SPVE in 2D altermagnets. Within a relativistic framework, symmetry analysis must incorporate magnetic symmetry operations that act concurrently on both spin and real-space coordinates. These operations define the constraints on the allowable components of the conductivity tensor $\sigma_{\text{shift/inj}}^{c,s^i;ab}$. To build a symmetry-guided theory for the SPVE in 2D altermagnets, we screened the 125 magnetic layer point groups [52], identifying 30 potential candidate targets. We then systematically classified the groups capable of supporting the SPVE to pinpoint candidate materials possessing the desired physical properties, as summarized in Table S1 of the SM.

More importantly, as the order parameter for altermagnets, the Néel vector provides a robust and non-volatile means of controlling magnetic symmetry. Consequently, the SPVE response remains strongly dependent on the orientation of the Néel vector and varies periodically as the vector is rotated. Guided by our theoretical

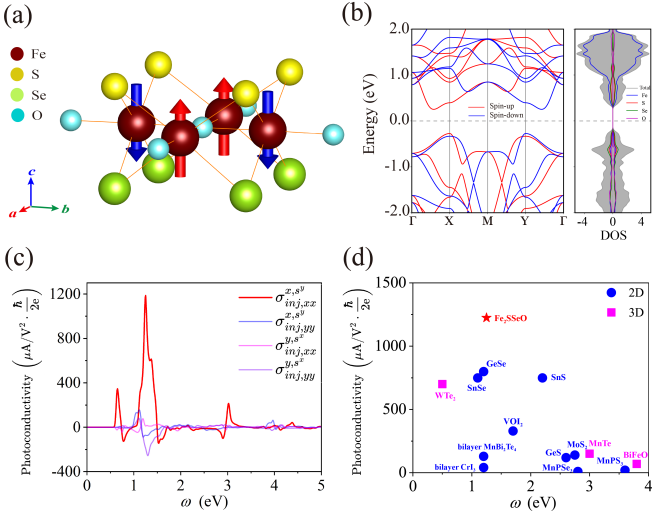


FIG. 2. (a) Crystal structure of Fe_2SSeO monolayer in the Néel type AFM configuration, with spin directions indicated by red (up) and blue (down) arrows. (b) Calculated band structure (without SOC) and spin-resolved PDOS for Fe_2SSeO monolayer, where red and blue denote spin-up and spin-down components, respectively. Regarding Fe_2SSeO monolayer, (c) Shown is the injection spin photoconductivity spectra computed with SOC for the Néel vector aligned along the [100] direction. (d) Performance comparison of the maximum spin current conductivity and its photon energy for Fe_2SSeO relative to selected 2D and 3D representative materials.

framework, we identified Fe_2SSeO as a representative altermagnetic system to validate the realization of a tunable giant spin injection current via the SPVE.

Material candidates.— In physics, many promising theoretical concepts have achieved significant progress, yet their practical implementation often hinges on the identification of suitable material candidates. The recent discovery of room-temperature metallic d -wave altermagnetism in layered vanadium oxytellurides $\text{Rb}_{1-\delta}\text{V}_2\text{Te}_2\text{O}$ and $\text{KV}_2\text{Se}_2\text{O}$ [53–55], combined with the successful experimental synthesis of layered iron oxychalcogenides $\text{BaFe}_2\text{Se}_2\text{O}$ and $\text{NaFe}_2\text{S}_2\text{O}$ [56–59], highlights the promise of this material family. Their pronounced van der Waals character motivates our investigation into their Janus monolayer derivatives.

Crystal structure of Janus Fe_2SSeO monolayer is illustrated in Fig. 2(a). The structure consists of a middle layer formed by transition metal Fe and oxygen atoms, sandwiched between a top S layer and a bottom Se layer, forming a characteristic Janus trait. The Janus Fe_2SSeO monolayer (space group No.99, $P4mm$) exhibits reduced symmetry due to broken out-of-plane mirror symmetry, while retaining tetrahedral coordination and in-plane \mathcal{C}_4 rotational symmetry. This material system has well-defined structural origins, and its single crystalline form can be derived from layered parent compounds. Using

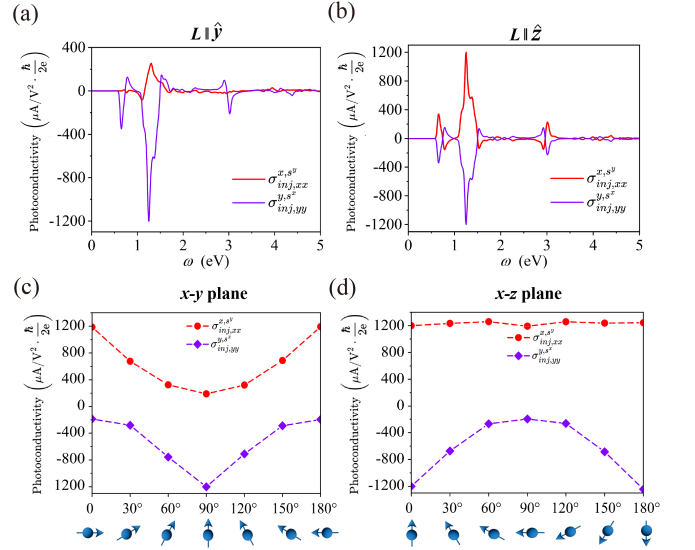


FIG. 3. (a-b) Injection spin photoconductivity components σ_{xx}^{xy} and σ_{yy}^{yx} under linearly polarized light, showcasing responses for polarization vectors along (a) $L \parallel \hat{y}$, (b) $L \parallel \hat{z}$. (c-d) Evolution of the nonlinear optical conductivities σ_{xx}^{xy} and σ_{yy}^{yx} in the (c) x - y plane and (d) x - z plane rotation angle α of the Néel vector.

Fe_2SSeO as a representative example, we systematically investigate the SPVE and its modulation mechanisms in 2D Janus altermagnets.

The calculated band structure and partial density of states (PDOS) of the Fe_2SSeO monolayer without considering SOC are shown in Fig. 2(b). Analysis reveals that Fe_2SSeO is an indirect bandgap semiconductor with a bandgap of 0.526 eV and exhibits significant spin splitting—a hallmark feature of altermagnetism. This behavior breaks the Kramers degeneracy commonly present in conventional \mathcal{PT} -antiferromagnets, leading to spin-split energy bands. These distinctive crystal and electronic properties make Fe_2SSeO an ideal candidate for exploring spin-dependent transport phenomena.

Switchable giant spin injection current.— The Janus Fe_2SSeO monolayer exhibits SPVE due to broken \mathcal{P} symmetry, enabling nonlinear spin current generation under optical excitation. Magnetic anisotropy calculations confirm soft magnetic behavior and identify an in-plane easy magnetization axis along the [100] direction (see Sec. IV of the SM), consistent with the magnetic point group $pm'm2'$. Applying the material’s symmetry operations to Eq. (2) yields independent tensor components for injection and shift spin currents (see Sec. V of the SM). Notably, although both spin currents are excited, their nonzero tensor elements are mutually independent and do not overlap. Under linearly polarized light, the independent nonzero components of the injection spin conductivity are σ_{xx}^{xy} , σ_{yy}^{yx} , σ_{xx}^{xx} , and σ_{yy}^{yy} . In contrast, the shift spin conductivity is constrained by \mathcal{T} symmetry:

TABLE I. Summary of the symmetry-allowed nonzero components for the linear shift and injection currents in Fe₂SSeO, evaluated for light polarization along the $L \parallel \hat{x}$, $L \parallel \hat{y}$, and $L \parallel \hat{z}$ directions.

Néel vector	Linear shift current	Linear injection current
$L \parallel \hat{x}$	$\sigma_{xx}^{xs^z}, \sigma_{yy}^{xs^z}$	$\sigma_{xx}^{xs^y}, \sigma_{yy}^{xs^y}, \sigma_{xx}^{ys^x}, \sigma_{yy}^{ys^x}$
$L \parallel \hat{y}$	$\sigma_{xx}^{ys^z}, \sigma_{yy}^{ys^z}$	$\sigma_{xx}^{xs^y}, \sigma_{yy}^{xs^y}, \sigma_{xx}^{ys^x}, \sigma_{yy}^{ys^x}$
$L \parallel \hat{z}$	$\sigma_{xx}^{xs^x} = -\sigma_{yy}^{ys^y}, \sigma_{yy}^{xs^x} = -\sigma_{xx}^{ys^y}$	$\sigma_{xx}^{xs^y} = -\sigma_{yy}^{ys^x}, \sigma_{yy}^{xs^y} = -\sigma_{xx}^{ys^x}$

the $\mathcal{M}_y\mathcal{T}$ operation nullifies the above four components, leaving only $\sigma_{xx}^{xs^z}$ and $\sigma_{yy}^{ys^z}$ as nonzero. This behavior arises from the coexistence of mirror and \mathcal{T} symmetries in the structure—a feature also observed in BPVE.

The NLO injection spin current conductivity of Fe₂SSeO monolayer under linearly polarized light [Fig. 2(c)] shows pronounced spectral features, with the $\sigma_{xx}^{xs^y}$ component exhibiting three distinct peaks in the $\omega = 0 \sim 5$ eV range. The most prominent peak, located at $\omega = 1.25$ eV, reaches a magnitude of $1224 \mu\text{A}/\text{V}^2\hbar/2e$, significantly exceeding values reported for other widely studied 2D and 3D materials [Fig. 2(d)] [40, 60–65]. Previous analysis indicates that $\sigma_{xx}^{xs^y}$ corresponds to injection current, while the other injection conductivity components $\sigma_{yy}^{xs^y}$, $\sigma_{xx}^{ys^x}$, and $\sigma_{yy}^{ys^x}$ are considerably smaller. As shown in Fig.S3, the shift conductivities $\sigma_{xx}^{xs^z}$ and $\sigma_{yy}^{ys^z}$ under linearly polarized light are also significantly lower than the injection terms, indicating that although both shift and injection spin currents are optically excited in monolayer Fe₂SSeO, the injection current dominates.

The SPVE exhibits strong sensitivity to the Néel vector orientation, as summarized in the Table I listing the non-zero components of σ for different Néel vector directions in Fe₂SSeO. Additionally, the spin currents generated under different linear polarizations can be interconnected through the unique crystal symmetry \mathcal{O} in altermagnets. When the magnetic axis is aligned along the [010] direction, the the 90° rotation of the Néel vector causes the large spin current originally carried by $\sigma_{xx}^{xs^y}$ to transform into the $\sigma_{yy}^{ys^x}$ component, accompanied by a sign reversal [Fig. 3(a)]. In contrast, when the magnetic axis is oriented along the [001] direction, the magnetic point group of the system changes to \mathcal{C}_{4z} rotational symmetry, which constrains $\sigma_{xx}^{xs^y} = -\sigma_{yy}^{ys^x}$, allowing both orientations to support a large spin current [Fig. 3(b)]. Figs. 3(c-d) further show the evolution of $\sigma_{xx}^{xs^y}$ and $\sigma_{yy}^{ys^x}$ in the x - y and x - z plane as the Néel vector rotates. Owing to the rotational symmetry of the crystal structure, the conductivity varies with a period of π , satisfying $\sigma(\alpha) = \sigma(\pi - \alpha)$. These results confirm that the spin current is strictly governed by the Néel vector orientation.

From the perspective of application, spin currents can be detected using established methods. For instance, in the spin Hall effect [4], an open-circuit configuration leads

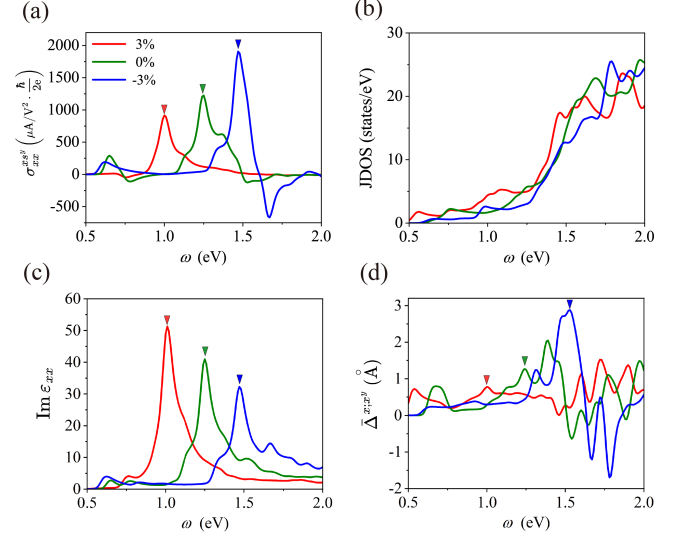


FIG. 4. (a) Injection spin current conductivity $\sigma_{xx}^{xs^y}$, (b) JDOS, (c) the absorptive part of the dielectric function $\text{Im} \varepsilon_{xx}$, and (d) aggregate injection vector $\bar{\Delta}^{x;y}$ as a function of the photon energy under different biaxial strain.

to spin accumulation at the sample edges, which can be measured via magneto-optical techniques such as Kerr rotation or the Faraday effect [66]. The strong dependence of the SPVE on Néel order makes monolayer Fe₂SSeO a highly promising candidate for designing SPVE-based spintronic devices.

Discussion and conclusion.— The development of effective approaches to manipulate nonlinear spin currents is essential for advancing functional material design and device applications. Strain engineering offers a versatile strategy for tuning material properties, applicable to thin films grown on a broad range of substrates [67–70], particularly through substrate-mediated tensile or compressive deformation. We further explored the effect of biaxial strain on the SPVE of Fe₂SSeO monolayer. As shown in Fig. 4(a), biaxial strain modulates the band structure, leading to distinct responses of the spin current conductivity $\sigma_{xx}^{xs^y}$ under tensile and compressive strains: tensile strain suppresses the conductivity and induces a red shift in the spectral peak, whereas compressive strain enhances the conductivity and leads to a blue shift. Notably, at -3% compressive strain, the peak conductivity

increases from $1224 \mu\text{A}/\text{V}^2 \cdot \hbar/2e$ ($\omega = 1.25 \text{ eV}$) to $1905 \mu\text{A}/\text{V}^2 \cdot \hbar/2e$ ($\omega = 1.47 \text{ eV}$). To understand the above features, we calculate three additional Brillouin zone integrated quantities: the joint density of states (JDOS) D_{joint} , the absorptive part of the dielectric function ε_{ab} , and the aggregate injection vector $\bar{\Delta}^{c;s^i}$ (detailed definitions are provided in the Sec.II. of the SM). As shown in Figs. 4(c) and 4(d), under strain modulation, both the ε_{xx} and the $\bar{\Delta}^{x;x^y}$ undergo changes, exhibiting a competitive relationship. However, the variation in the injection vector dominates, leading to a notable enhancement of conductivity under compressive strain and the opposite under tensile strain. This enhancement can be attributed to shortened interatomic distances and a strengthened built-in electric field under compression, which facilitate carrier transport and spin current generation.

In summary, we have established a generalized symmetry-based framework for the SPVE under linearly polarized light in conventional \mathcal{PT} -antiferromagnets and Janus altermagnets. Our analysis shows that under linearly polarized light excitation, Janus altermagnets support both shift and injection spin photocurrents, whereas only shift currents are allowed in \mathcal{PT} -antiferromagnets. Using Janus Fe_2SSeO monolayer as a representative example, we demonstrated a giant polarization-dependent injection current, with a conductivity of $1224 \mu\text{A}/\text{V}^2 \cdot \hbar/2e$ in Fe_2SSeO —one to two orders of magnitude larger than typical 2D materials. The SPVE response is highly sensitive to the Néel vector orientation, showing π -periodic modulation upon its rotation, and can be further tuned via biaxial strain. The observed giant and switchable spin photocurrent underscores the potential of Janus altermagnets for applications in nonlinear optoelectronics and optical spintronics.

* zhangrunwu@bit.edu.cn

† lilei1993@imu.edu.cn

- [1] I. Žutić, J. Fabian, and S. D. Sarma, Spintronics: Fundamentals and applications, *Rev. Mod. Phys.* **76**, 323 (2004).
- [2] S. D. Bader and S. S. P. Parkin, Spintronics, *Annu. Rev. Condens. Matter Phys.* **1**, 71 (2010).
- [3] D. D. Awschalom and M. E. Flatté, Challenges for semiconductor spintronics, *Nat. Phys.* **3**, 153 (2007).
- [4] J. Sinova, S. O. Valenzuela, J. Wunderlich, C. H. Back, and T. Jungwirth, Spin hall effects, *Rev. Mod. Phys.* **87**, 1213 (2015).
- [5] V. Baltz, A. Manchon, M. Tsoi, T. Moriyama, T. Ono, and Y. Tserkovnyak, Antiferromagnetic spintronics, *Rev. Mod. Phys.* **90**, 015005 (2018).
- [6] T. D. Ladd, F. Jelezko, R. Laflamme, Y. Nakamura, C. Monroe, and J. L. O'Brien, Quantum computers, *Nature* **464**, 45 (2010).
- [7] S. Umesh and S. Mittal, A survey of spintronic architectures for processing-in-memory and neural networks, *J. Syst. Archit.* **97**, 349 (2019).
- [8] M. I. Dyakonov and V. Perel, Current-induced spin orientation of electrons in semiconductors, *Phys. Lett. A* **35**, 459 (1971).
- [9] S. Murakami, N. Nagaosa, and S.-C. Zhang, Dissipationless quantum spin current at room temperature, *Science* **301**, 1348 (2003).
- [10] J. Sinova, D. Culcer, Q. Niu, N. Sinitsyn, T. Jungwirth, and A. H. MacDonald, Universal intrinsic spin Hall effect, *Phys. Rev. Lett.* **92**, 126603 (2004).
- [11] C. L. Kane and E. J. Mele, Quantum spin Hall effect in graphene, *Phys. Rev. Lett.* **95**, 226801 (2005).
- [12] B. A. Bernevig and S.-C. Zhang, Quantum spin Hall effect, *Phys. Rev. Lett.* **96**, 106802 (2006).
- [13] L. Li, C. Cui, R.-W. Zhang, Z.-M. Yu, and Y. Yao, Planar Hall plateau in magnetic Weyl semimetals, *Sci. Bull.* **70**, 187 (2025).
- [14] R. Cheng, J. Xiao, Q. Niu, and A. Brataas, Spin pumping and spin-transfer torques in antiferromagnets, *Phys. Rev. Lett.* **113**, 057601 (2014).
- [15] W. Zhang, M. B. Jungfleisch, W. Jiang, J. E. Pearson, A. Hoffmann, F. Freimuth, and Y. Mokrousov, Spin Hall effects in metallic antiferromagnets, *Phys. Rev. Lett.* **113**, 196602 (2014).
- [16] H. Wang, C. Du, P. C. Hammel, and F. Yang, Antiferromagnonic spin transport from $\text{Y}_3\text{Fe}_5\text{O}_{12}$ into NiO, *Phys. Rev. Lett.* **113**, 097202 (2014).
- [17] L. Frangou, S. Oyarzun, S. Auffret, L. Vila, S. Gambarelli, and V. Baltz, Enhanced spin pumping efficiency in antiferromagnetic IrMn thin films around the magnetic phase transition, *Phys. Rev. Lett.* **116**, 077203 (2016).
- [18] S. Rezende, R. Rodríguez-Suárez, and A. Azevedo, Diffusive magnonic spin transport in antiferromagnetic insulators, *Phys. Rev. B* **93**, 054412 (2016).
- [19] T. Jungwirth, X. Marti, P. Wadley, and J. Wunderlich, Antiferromagnetic spintronics, *Nat. Nanotechnol.* **11**, 231 (2016).
- [20] R. Lebrun, A. Ross, S. Bender, A. Qaiumzadeh, L. Baldrati, J. Cramer, A. Brataas, R. Duine, and M. Kläui, Tunable long-distance spin transport in a crystalline antiferromagnetic iron oxide, *Nature* **561**, 222 (2018).
- [21] A. Manchon, J. Železný, I. M. Miron, T. Jungwirth, J. Sinova, A. Thiaville, K. Garello, and P. Gambardella, Current-induced spin-orbit torques in ferromagnetic and antiferromagnetic systems, *Rev. Mod. Phys.* **91**, 035004 (2019).
- [22] D. Hou, Z. Qiu, and E. Saitoh, Spin transport in antiferromagnetic insulators: progress and challenges, *NPG Asia Mater.* **11**, 35 (2019).
- [23] S. Hayami, Y. Yanagi, and H. Kusunose, Momentum-dependent spin splitting by collinear antiferromagnetic ordering, *J. Phys. Soc. Jpn.* **88**, 123702 (2019).
- [24] L. Šmejkal, J. Sinova, and T. Jungwirth, Emerging research landscape of altermagnetism, *Phys. Rev. X* **12**, 040501 (2022).
- [25] D. Zhu, Z.-Y. Zhuang, Z. Wu, and Z. Yan, Topological superconductivity in two-dimensional altermagnetic metals, *Phys. Rev. B* **108**, 184505 (2023).
- [26] L. Bai, W. Feng, S. Liu, L. Šmejkal, Y. Mokrousov, and Y. Yao, Altermagnetism: Exploring new frontiers in magnetism and spintronics, *Adv. Funct. Mater.* **34**, 2409327 (2024).
- [27] S. Lee, S. Lee, S. Jung, J. Jung, D. Kim, Y. Lee, B. Seok, J. Kim, B. G. Park, L. Šmejkal, *et al.*, Broken Kramers

- degeneracy in altermagnetic MnTe, *Phys. Rev. Lett.* **132**, 036702 (2024).
- [28] X. Zhou, W. Feng, R.-W. Zhang, L. Šmejkal, J. Sinova, Y. Mokrousov, and Y. Yao, Crystal thermal transport in altermagnetic RuO₂, *Phys. Rev. Lett.* **132**, 056701 (2024).
- [29] J. Krempaský, L. Šmejkal, S. D'souza, M. Hajlaoui, G. Springholz, K. Uhlířová, F. Alarab, P. Constantinou, V. Strocov, D. Usanov, *et al.*, Altermagnetic lifting of Kramers spin degeneracy, *Nature* **626**, 517 (2024).
- [30] S. Reimers, L. Odenbreit, L. Šmejkal, V. N. Strocov, P. Constantinou, A. B. Hellenes, R. Jaeschke Ubiergo, W. H. Campos, V. K. Bharadwaj, A. Chakraborty, *et al.*, Direct observation of altermagnetic band splitting in CrSb thin films, *Nat. Commun.* **15**, 2116 (2024).
- [31] R.-W. Zhang, C. Cui, R. Li, J. Duan, L. Li, Z.-M. Yu, and Y. Yao, Predictable gate-field control of spin in altermagnets with spin-layer coupling, *Phys. Rev. Lett.* **133**, 056401 (2024).
- [32] T. He, L. Li, C. Cui, R.-W. Zhang, Z.-M. Yu, G. Liu, and X. Zhang, Quasi-one-dimensional spin transport in altermagnetic Z_3 nodal net metals, *Phys. Rev. Lett.* **133**, 146602 (2024).
- [33] H.-Z. Zhang, C. Cui, J. Duan, T. He, and R.-W. Zhang, Tunable anisotropic crystal spin transport in two-dimensional altermagnetic transition metal oxychalcogenides, *Mater. Horiz.* **12**, 9282 (2025).
- [34] S. D. Ganichev, E. Ivchenko, V. Bel'Kov, S. Tarasenko, M. Sollinger, D. Weiss, W. Wegscheider, and W. Prettl, Spin-galvanic effect, *Nature* **417**, 153 (2002).
- [35] R. R. Bhat, F. Nastos, A. Najmaie, and J. Sipe, Pure Spin Current from One-Photon Absorption of Linearly Polarized Light in Noncentrosymmetric Semiconductors, *Phys. Rev. Lett.* **94**, 096603 (2005).
- [36] B. Zhou and S.-Q. Shen, Deduction of pure spin current from the linear and circular spin photogalvanic effect in semiconductor quantum wells, *Phys. Rev. B* **75**, 045339 (2007).
- [37] S. M. Young, F. Zheng, and A. M. Rappe, Prediction of a linear spin bulk photovoltaic effect in antiferromagnets, *Phys. Rev. Lett.* **110**, 057201 (2013).
- [38] H. Xu, H. Wang, J. Zhou, and J. Li, Pure spin photocurrent in non-centrosymmetric crystals: bulk spin photovoltaic effect, *Nat. Commun.* **12**, 4330 (2021).
- [39] R. Fei, W. Song, L. Pusey-Nazzaro, and L. Yang, PT-symmetry-enabled spin circular photogalvanic effect in antiferromagnetic insulators, *Phys. Rev. Lett.* **127**, 207402 (2021).
- [40] R.-C. Xiao, D.-F. Shao, Y.-H. Li, and H. Jiang, Spin photogalvanic effect in two-dimensional collinear antiferromagnets, *npj Quantum Mater.* **6**, 35 (2021).
- [41] H. Wang and X. Qian, Ferroicity-driven nonlinear photocurrent switching in time-reversal invariant ferroic materials, *Sci. Adv.* **5**, eaav9743 (2019).
- [42] J. Ahn, G.-Y. Guo, and N. Nagaosa, Low-frequency divergence and quantum geometry of the bulk photovoltaic effect in topological semimetals, *Phys. Rev. X* **10**, 041041 (2020).
- [43] H. Watanabe and Y. Yanase, Chiral photocurrent in parity-violating magnet and enhanced response in topological antiferromagnet, *Phys. Rev. X* **11**, 011001 (2021).
- [44] N. Nagaosa and Y. Yanase, Nonreciprocal transport and optical phenomena in quantum materials, *Annu. Rev. Condens. Matter Phys.* **15**, 63 (2024).
- [45] R. von Baltz and W. Kraut, Theory of the bulk photovoltaic effect in pure crystals, *Phys. Rev. B* **23**, 5590 (1981).
- [46] J. Sipe and A. Shkrebti, Second-order optical response in semiconductors, *Phys. Rev. B* **61**, 5337 (2000).
- [47] V. I. Belinicher and B. I. Sturman, The photogalvanic effect in media lacking a center of symmetry, *Sov. Phys. Usp.* **23**, 199 (1980).
- [48] S. V. Gallego, J. Etxebarria, L. Elcoro, E. S. Tasci, and J. M. Perez-Mato, Automatic calculation of symmetry-adapted tensors in magnetic and non-magnetic materials: a new tool of the Bilbao Crystallographic Server, *Acta Crystallogr. A* **75**, 438 (2019).
- [49] T. Holder, D. Kaplan, and B. Yan, Consequences of time-reversal-symmetry breaking in the light-matter interaction: Berry curvature, quantum metric, and diabatic motion, *Phys. Rev. Res.* **2**, 033100 (2020).
- [50] N. D. Mermin and H. Wagner, Absence of ferromagnetism or antiferromagnetism in one- or two-dimensional isotropic Heisenberg models, *Phys. Rev. Lett.* **17**, 1133 (1966).
- [51] B. I. Halperin, On the Hohenberg–Mermin–Wagner theorem and its limitations, *J. Stat. Phys.* **175**, 521 (2019).
- [52] Y. Wang, C. Cui, Y. Han, T. He, W. Wu, R.-W. Zhang, Z.-M. Yu, S. A. Yang, and Y. Yao, Type-II Antiferroelectricity, arXiv preprint arXiv:2507.20285 (2025).
- [53] A. Ablimit, Y.-L. Sun, H. Jiang, S.-Q. Wu, Y.-B. Liu, and G.-H. Cao, Weak metal-metal transition in the vanadium oxytelluride Rb_{1- δ} V₂Te₂O, *Phys. Rev. B* **97**, 214517 (2018).
- [54] F. Zhang, X. Cheng, Z. Yin, C. Liu, L. Deng, Y. Qiao, Z. Shi, S. Zhang, J. Lin, Z. Liu, *et al.*, Crystal-symmetry-paired spin–valley locking in a layered room-temperature metallic altermagnet candidate, *Nat. Phys.* **21**, 760 (2025).
- [55] B. Jiang, M. Hu, J. Bai, Z. Song, C. Mu, G. Qu, W. Li, W. Zhu, H. Pi, Z. Wei, *et al.*, A metallic room-temperature d-wave altermagnet, *Nat. Phys.* **21**, 754 (2025).
- [56] J. He, D. Wang, H. Shi, H. Yang, J. Li, and G. Chen, Synthesis, structure, and magnetic properties of the layered iron oxychalcogenide NaFe₂Se₂O, *Phys. Rev. B* **84**, 205212 (2011).
- [57] H. Lei, H. Ryu, V. Ivanovski, J. Warren, A. Frenkel, B. Cekic, W.-G. Yin, and C. Petrovic, Structure and physical properties of the layered iron oxychalcogenide BaFe₂Se₂O, *Phys. Rev. B* **86**, 195133 (2012).
- [58] F. Takeiri, Y. Matsumoto, T. Yamamoto, N. Hayashi, Z. Li, T. Tohyama, C. Tassel, C. Ritter, Y. Narumi, M. Hagiwara, *et al.*, High-pressure synthesis of the layered iron oxyselenide BaFe₂Se₂O with strong magnetic anisotropy, *Phys. Rev. B* **94**, 184426 (2016).
- [59] S.-J. Song, J.-Y. Lu, Q.-Q. Zhu, Z. Ren, and G.-H. Cao, Crystal structure and physical properties of layered NaFe₂S₂O, *J. Phys. Chem. Solids* **181**, 111469 (2023).
- [60] X. Mu, Y. Pan, and J. Zhou, Pure bulk orbital and spin photocurrent in two-dimensional ferroelectric materials, *npj Comput. Mater.* **7**, 61 (2021).
- [61] H. Xu, H. Wang, and J. Li, Abnormal nonlinear optical responses on the surface of topological materials, *npj Comput. Mater.* **8**, 111 (2022).
- [62] Q. Xue, X. Mu, Y. Sun, and J. Zhou, Valley contrasting bulk photovoltaic effect in a \mathcal{PT} -symmetric MnPSe₃ monolayer, *Phys. Rev. B* **107**, 245404 (2023).

- [63] C. Liao, M. Wang, and Y.-J. Zhao, Enormous and Tunable Bulk Charge/Spin Photovoltaic Effect in Piezoelectric Binary Materials T-IV-VI and T-V-V, *J. Phys. Chem. Lett.* **15**, 6099 (2024).
- [64] R. Dong, R. Cao, D. Tan, and R. Fei, Crystal symmetry selected pure spin photocurrent in altermagnetic insulators, *Phys. Rev. B* **111**, 195210 (2025).
- [65] Y. Yang, Giant bulk spin photovoltaic effect in the two-dimensional altermagnetic multiferroics VOX₂, *Phys. Rev. B* **112**, 104427 (2025).
- [66] Y. K. Kato, R. C. Myers, A. C. Gossard, and D. D. Awschalom, Observation of the spin hall effect in semiconductors, *Science* **306**, 1910 (2004).
- [67] S. Nadupalli, J. Kreisel, and T. Granzow, Increasing bulk photovoltaic current by strain tuning, *Sci. Adv.* **5**, eaau9199 (2019).
- [68] A. M. Schankler, L. Gao, and A. M. Rappe, Large bulk piezophotovoltaic effect of monolayer 2H-MoS₂, *J. Phys. Chem. Lett.* **12**, 1244 (2021).
- [69] Y. Dong, M.-M. Yang, M. Yoshii, S. Matsuoka, S. Kitamura, T. Hasegawa, N. Ogawa, T. Morimoto, T. Ideue, and Y. Iwasa, Giant bulk piezophotovoltaic effect in 3R-MoS₂, *Nat. Nanotechnol.* **18**, 36 (2023).
- [70] L. Yang, L. Li, Z.-M. Yu, M. Wu, and Y. Yao, Two-dimensional topological ferroelectric metal with giant shift current, *Phys. Rev. Lett.* **133**, 186801 (2024).